Cavity-mediated iSWAP oscillations between distant spins

Dijkema, Jurgen; Xue, Xiao; Harvey-Collard, Patrick; Rimbach-Russ, Maximilian; de Snoo, Sander L.; Zheng, Guoji; Sammak, Amir; Scappucci, Giordano; Vandersypen, Lieven M.K.

DOI
10.1038/s41567-024-02694-8

Publication date
2024

Document Version
Final published version

Published in
Nature Physics

Citation (APA)
Dijkema, J., Xue, X., Harvey-Collard, P., Rimbach-Russ, M., de Snoo, S. L., Zheng, G., Sammak, A., Scappucci, G., & Vandersypen, L. M. K. (2024). Cavity-mediated iSWAP oscillations between distant spins. *Nature Physics*, *21*(1), 168-174. Article 13575. https://doi.org/10.1038/s41567-024-02694-8

nature physics

Article

https://doi.org/10.1038/s41567-024-02694-8

Cavity-mediated iSWAP oscillations between distant spins

Received: 29 July 2024

Accepted: 7 October 2024

Jurgen Dijkema[1,3], Xiao Xue[1,3], Patrick Harvey-Collard[1], Maximilian Rimbach-Russ[1], Sander L. de Snoo[1], Guoji Zheng[1], Amir Sammak[2], Giordano Scappucci[1] & Lieven M. K. Vandersypen[1] ✉

Direct interactions between quantum particles naturally fall off with distance. However, future quantum computing architectures are likely to require interaction mechanisms between qubits across a range of length scales. In this work, we demonstrate a coherent interaction between two semiconductor spin qubits 250 μm apart using a superconducting resonator. This separation is several orders of magnitude larger than for the commonly used direct interaction mechanisms in this platform. We operate the system in a regime in which the resonator mediates a spin–spin coupling through virtual photons. We report the anti-phase oscillations of the populations of the two spins with controllable frequency. The observations are consistent with iSWAP oscillations of the spin qubits, and suggest that entangling operations are possible in 10 ns. These results hold promise for scalable networks of spin qubit modules on a chip.

Solving relevant problems with quantum computers will require millions of error-corrected qubits[1]. Efforts across quantum computing platforms based on superconducting qubits, trapped ions and colour centres target a modular architecture for overcoming the obstacles to scaling, with modules on separate chips or boards, or even in separate vacuum chambers or refrigerators[2]. For semiconductor spin qubits[3,4], the small qubit footprint together with the capabilities of advanced semiconductor manufacturing[5,6] may enable a large-scale modular processor integrated on a single chip[7].

Semiconductor spin qubits are most commonly realized by confining individual electrons or holes in electrostatically defined quantum dots. Nearly all quantum logic demonstrations between such qubits are based on the exchange interaction that arises from wavefunction overlap between charges in neighbouring dots, with typical qubit separations of 100–200 nm (refs. 4,8). The monolithic integration of a million-qubit register at a 100 nm pitch will face challenges, related to the fan-out of control and readout wires. Combining local exchange-based gates and operations between qubits 10 μm to 250 μm apart provides a path to on-chip interconnected modules[7,9]. Various approaches for two-qubit operations over larger distances have been pursued, such as coupling spins via an intermediate quantum dot[10,11], capacitive coupling[12] and shuttling of electrons, propelled either by gate voltages[13,14] or by surface acoustic waves[15]. However, the first two methods are still limited to submicrometre distances and the use of surface acoustic waves faces many practical obstacles, especially in group IV semiconductors. Electrically controlled shuttling, although regarded as a promising route, is relatively slow, and therefore, the coupling distance is constrained by the relevant coherence times. On the other hand, integrating spin qubits with on-chip superconducting resonators using the circuit quantum electrodynamics framework provides an elegant way of constructing an on-chip network[16,17]. With this approach, coupling distances of several hundreds of micrometres are achievable and operations can be just as fast as those based on wavefunction overlap.

In recent years, strong spin–photon coupling[18–20] and resonant spin–photon–spin coupling[21] have both been reported in hybrid dot–resonator devices. Among the many ways for constructing distant quantum gates in this architecture[17], coupling the spins dispersively via virtual photons looks highly promising[22,23]. In this regime, the frequencies of the two qubits are detuned from the resonator frequency and the leakage of quantum information into resonator photons is largely suppressed[24,25]. Spin–spin coupling in the dispersive regime has been observed recently in spectroscopy[26], but two-qubit oscillations in the time domain remains to be demonstrated. Furthermore,

---

[1] QuTech and Kavli Institute of Nanoscience, Delft University of Technology, Delft, Netherlands. [2] QuTech and Netherlands Organization for Applied Scientific Research (TNO), Delft, Netherlands. [3] These authors contributed equally: Jurgen Dijkema, Xiao Xue. ✉e-mail: l.m.k.vandersypen@tudelft.nl

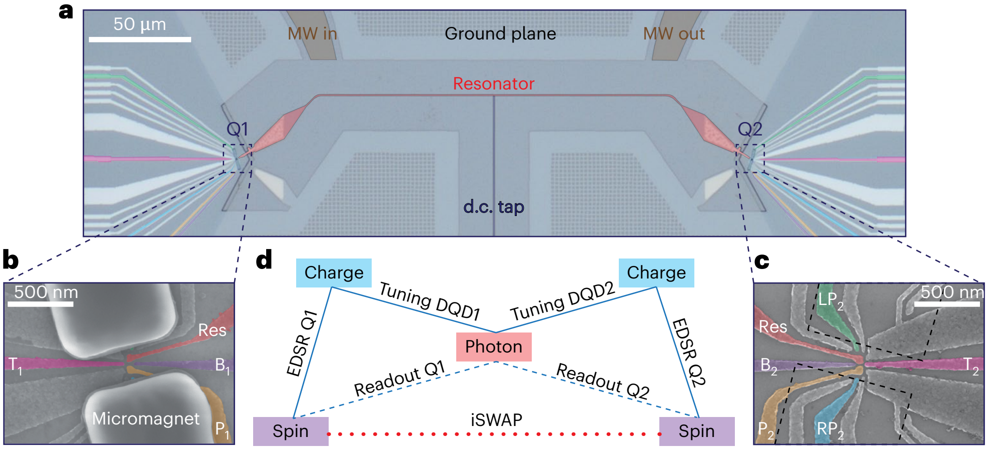

Fig. 1 | Dot–resonator–dot device. **a**, False-coloured optical image of the device that is used in this work, showing the resonator, ground planes and gate fan-out of the DQDs. The microwave (MW) in/out ports are used to probe the transmission through the resonator, and the d.c. tap is used to bias the shared top-gate Res (in **b** and **c**) of the two DQDs. **b**, Scanning electron microscopy image of a DQD with the same design as the measured DQD_1, showing the gate pattern and micromagnets on top. **c**, Scanning electron microscopy image of a similar DQD without micromagnets to show the full gate layout of DQD_2. The dashed lines outline the micromagnets of the measured device. The false-coloured gates in **b** and **c** are plunger gates Res and P_i, tunnel-barrier gates B_i and T_i, and side gates RP_i and LP_i. **d**, Schematic of the distant spin–spin coupling architecture. The blue and red lines indicate the dispersive and resonant couplings, respectively. The solid lines represent direct couplings, which are the charge–photon electric-dipole coupling and the spin–charge coupling enabled by the micromagnet gradients. These couplings are utilized for probing the DQD charge susceptibility, which allows us to tune the DQD to the degeneracy point and for electric-dipole spin resonance, respectively. The dashed lines indicate the indirect spin–photon couplings that enable dispersive spin readout. The dotted line indicates a second-order indirect coupling, that is, the spin–spin coupling mediated by virtual photons, which enables iSWAP oscillations.

in colour centres[27] and self-assembled quantum dots[28], the observation of cavity-mediated spin–spin evolution presents an outstanding challenge.

In this work, we demonstrate the time-domain control of a dot–resonator–dot system and realize two-qubit iSWAP oscillations between distant spin qubits. The two qubits are encoded in single-electron spin states and they are coupled via a 250-µm-long superconducting NbTiN on-chip resonator. The resonator is also used for dispersively probing the spin states[18,29]. First, we demonstrate operations on individual spin qubits at the flopping-mode operating point[30,31] and characterize the corresponding coherence times. Then, we realize iSWAP oscillations between the two distant spin qubits in the dispersive regime. We study how the oscillation frequency varies with spin–cavity detuning, spin–photon coupling strength and frequency detuning between the two spin qubits, and compare the results with theoretical simulations.

Device

The device is fabricated on a ^{28}Si/SiGe heterostructure and was used in a previous experiment to demonstrate dispersive spin–spin coupling via spectroscopic measurements[26]. It contains an on-chip superconducting resonator with an impedance of 3 kΩ (ref. 32) and a double quantum dot (DQD) at both ends, with gate filters[33] (Fig. 1a). The resonator is etched out of a 5- to 7-nm thick NbTiN film, and is 250 µm long. Its fundamental half-wave mode, with $\omega_r/2\pi = 6.9105$ GHz and a linewidth of $\kappa_r/2\pi = 1.8$ MHz ($Q \approx 3{,}800$), is used in the experiment for both long-range coupling and dispersive spin readout. The DQD is defined by a single layer of Al gate electrodes (Fig. 1c). The gates labelled Res are galvanically connected to the resonator. On top of each DQD, a pair of cobalt micromagnets is deposited (Fig. 1b). The device is mounted on a printed circuit board attached to the mixing chamber of a dilution refrigerator with a base temperature of 8 mK (Supplementary Section B provides additional details on the experimental setup).

We accumulate electrons in the DQD_i ($i = 1, 2$) via plunger gates Res and P_i. The interdot tunnel couplings are controlled by the tunnel-barrier gates, labelled T_i and B_i. The side gates RP_i and LP_i are used to control the electrochemical potentials and thus the detuning for each DQD. In the time-domain experiments, we pulse the detunings via the RP_i gates and drive single qubits by applying microwave bursts through the LP_i gates. The d.c. voltages on these gates are chosen such that DQD_1 is at the degeneracy point between the (1,0)–(0,1) charge configuration, whereas DQD_2 is at (3,2)–(2,3) to reach the desired tunnel coupling with modest gate voltages ((m, n) indicate the number of electrons in each DQD). Both DQDs are tuned to a similar tunnel coupling of ~4.8 GHz. At the charge degeneracy point, the electron is delocalized between the two dots and the resulting charge dipole is maximized[34], enabling a charge–photon coupling strength of ~192 MHz for both DQDs. The magnetic-field gradient produced by the micromagnets results in the hybridization of spin and charge states, which allows an indirect electric-dipole interaction between the photons and spins (Fig. 1d). The spin–photon coupling can be effectively switched off by pulsing the detuning via the RP_i gate, to an operating point at which the electron is tightly localized in a single dot and its electric susceptibility is suppressed. The micromagnets are tilted by ±15° relative to the double-dot axis, which permits tuning the Zeeman energy difference between the two spin qubits by rotating the external magnetic field[21]. In the presence of an external magnetic field B_{ext} of 50 mT and at an angle of 4.7°, both qubits are set to a frequency of ~6.82 GHz, slightly detuned from the resonator frequency. The two spins then resonantly interact with each other, mediated by virtual photons in the resonator (Fig. 1d).

Flopping-mode qubits

We first separately examine the individual qubits located at both ends of the resonator. We encode the qubits in two eigenstates at the charge degeneracy point: $|-,\downarrow\rangle$ as logical $|0\rangle$ and $\alpha|-,\uparrow\rangle + \beta|+,\downarrow\rangle$ as logical $|1\rangle$. Here $|\downarrow\rangle/|\uparrow\rangle$ is the spin state, $|-\rangle/|+\rangle$ is the bonding/antibonding orbital and the coefficient $\alpha/\beta \gg 1$ is determined by the degree of spin–charge hybridization[35,36] ($|\pm\rangle = (|L\rangle \pm |R\rangle)/\sqrt{2}$, where $|L\rangle/|R\rangle$ indicates the state in which an electron occupies the left/right dot, respectively). The qubits are manipulated using electric-dipole spin resonance (EDSR) enabled by the micromagnets[37]. Operation at the charge degeneracy point, chosen to maximize the charge–photon and spin–photon coupling strengths, implies that even the EDSR Rabi frequencies are

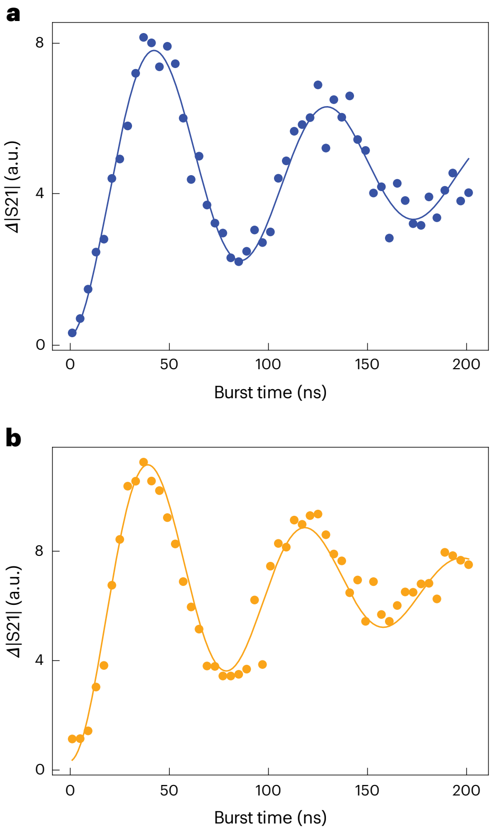

Fig. 2 | Rabi oscillations in flopping mode. a,**b**, Rabi oscillations for qubit 1 (**a**) and qubit 2 (**b**), driven in the flopping-mode regime. The measured transmission through the resonator as a function of the applied MW burst time, resonant with qubit 1 and qubit 2, is shown by the data points. The solid lines represent fits to the data with a damped sinusoid. From the fits, we extract a Rabi decay time T_2^{Rabi} of 100 ns and 120 ns for the two qubits. Although experimenting on one qubit, the other qubit is parked in the left dot of the corresponding DQD, and therefore, its coupling to the resonator is effectively switched off. Each data point is averaged for 10^5 times.

maximized, since they rely on the same matrix element (Fig. 1d). This regime is also known as the flopping-mode regime[31]. Furthermore, since the detuning between the spin and cavity is larger than the spin–photon coupling strength (as shown below), the spin qubit state is only weakly hybridized with the photons.

Spin readout is natively achieved in the regime of dispersive spin–photon coupling given that the resonator frequency depends on the electron's spin state. To detect the spin states, we send a microwave probe signal to the resonator at a frequency corresponding to the resonator's frequency with the qubit in $|0\rangle$. In all the measurements, the change in microwave transmission (termed transmission for short) relative to this reference value is used as a measure of the $|1\rangle$ population. Due to the limited qubit relaxation times (discussed later), the $|1\rangle$ signal decays within hundreds of nanoseconds. Even though we use a travelling-wave parametric amplifier[38] to increase the signal-to-noise ratio, signal averaging over many cycles is needed (Supplementary Section A provides a detailed explanation of the read-out procedure).

For qubit initialization, we rely on spontaneous relaxation to the ground state. For this purpose, the short relaxation timescales at the charge degeneracy point are helpful. In practice, a waiting time of 1 µs is sufficient for initialization ($\geq 5T_1$).

Time-domain single-qubit control of both qubits is illustrated in Fig. 2. We repeatedly initialize the qubit to $|0\rangle$, apply a resonant microwave burst of variable duration through gate LP$_i$ and successively measure both qubits. Although we measure one qubit, we pulse the detuning of the other qubit away from the charge degeneracy point so that it does not affect the transmission through the resonator. When we plot the average transmission versus microwave burst time, we observe a damped oscillation, as expected.

Using standard pulse sequences, we next characterize the relaxation and decoherence times of the spin qubits in this system (Supplementary Table 1). The relaxation (T_1) and dephasing (T_2^*) times, which range from 100 ns to 260 ns and 40 ns to 80 ns, respectively, do not match the state-of-the-art spin qubit benchmarks[39]. This is expected given the strong spin–charge hybridization at the charge degeneracy point, making the qubits highly sensitive to charge noise[30]. This is the flip side of the faster Rabi oscillations and stronger spin–photon coupling at this working point. Additional contributions to relaxation arise from the Purcell decay induced by the resonator[40] (Extended Data Fig. 1), and additional decoherence sources include the residual photon population induced by the readout signals[41] and intrinsic slow electrical drift in this device.

Two-qubit interaction

The spin–spin interaction in the dispersive regime, with both spins resonant with each other but detuned from the resonator, is described by the Tavis–Cummings Hamiltonian[42]. This Hamiltonian describes the collective qubit coupling with a resonator and can be simplified to the following dispersive spin–spin coupling Hamiltonian in the rotating-wave approximation[22,43]:

$$H \approx \hbar J\left(\sigma_{+,1}\sigma_{-,2} + \sigma_{-,1}\sigma_{+,2}\right), \tag{1}$$

where J is the effective spin–spin coupling strength and $\sigma_{\pm,i}$ denote the usual raising and lowering operators for qubit i. The coupling strength is given by

$$2J = g_{\mathrm{s},1}g_{\mathrm{s},2}\left(\frac{1}{\Delta_{2\mathrm{s},1}} + \frac{1}{\Delta_{2\mathrm{s},2}}\right), \tag{2}$$

where $g_{\mathrm{s},1}$ and $g_{\mathrm{s},2}$ are the spin–photon coupling strengths for spins 1 and 2, respectively. $\Delta_{2\mathrm{s},1(2)}$ describes the detuning between the frequency of qubit 1 (2) and the loaded cavity frequency. The interaction with the two charge dipoles dispersively shifts the cavity frequency away from its bare frequency, to ~6.884 GHz when both electrons interact with the cavity (both DQDs at charge degeneracy) and to ~6.897 GHz when only one electron is coupled[26].

The Hamiltonian of equation (1) generates iSWAP oscillations between the two spins. We probe this dynamics operating for now in a regime in which $g_{\mathrm{s},1(2)}/2\pi \approx 21.5$ MHz and $\Delta_{2\mathrm{s},1(2)}/2\pi \approx 65.5$ MHz. Both spins are initialized to $|0\rangle$ by waiting for 1 µs at zero detuning (Fig. 3a,c). Next, one of the spins is prepared in $|1\rangle$, using a calibrated π-pulse in the flopping mode, whereas the other spin is pulsed away from charge degeneracy to effectively decouple it from the cavity (Extended Data Fig. 2 shows the initialization in a single dot). The spins are then allowed to interact with each other by pulsing the second spin back to charge degeneracy, at which point the spins are resonant with each other but still detuned from the (loaded) cavity. After a variable interaction time t_{int}, the spins are read out sequentially, once again with the other spin decoupled from the cavity.

Figure 3b(d) shows the measured evolution of both spins starting from $|10\rangle$ ($|01\rangle$). The populations evolve periodically in anti-phase in both experiments, as expected for coherent iSWAP oscillations. The extracted oscillation frequencies are ~11.7 MHz (Fig. 3b,d). The populations of the two spins, separated by more than 200 µm, are exchanged in just ~42 ns. A coupling time of ~21 ns is expected to maximally entangle the spins, based on equation (1). The fidelity of the entangling operation in this regime is numerically estimated to be 83.1% (Extended Data Fig. 3 and Supplementary Section D). The number of visible periods is limited due to the comparatively fast decoherence.

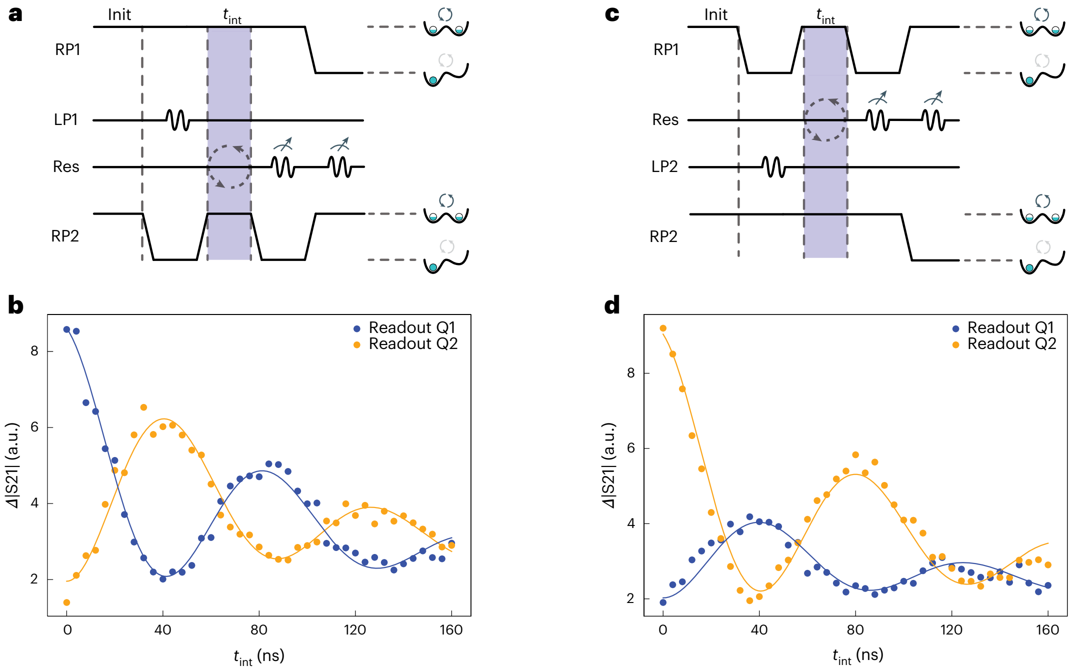

Fig. 3 | iSWAP oscillations between two distant spin qubits. a, Pulse sequence for the measurement of iSWAP oscillations starting from |10⟩. The two qubits are initialized in |00⟩ by relaxation at the charge degeneracy point. Then, qubit 2 is isolated in the left dot for 500 ns, during which a π-pulse is applied to qubit 1. After 10 ns, qubit 2 is pulsed back into interaction, and both spins interact with each other for t_{int}. After the interaction interval, qubit 2 is isolated in its left dot for 1 μs, where relaxation is expected to be slower, whereas qubit 1 is read out using a 400-ns-long probe tone. Subsequently, qubit 1 is isolated in its left dot and qubit 2 is read out using a 400 ns probe tone. **b**, The data points show the measured (change in) transmission, representative of the spin-up population for each spin, starting from |10⟩. Each data point is averaged for 10^6 times. Here $g_{\mathrm{s},1(2)}/2\pi \approx 21.5$ MHz and $\Delta_{2\mathrm{s},1(2)}/2\pi \approx 65.5$ MHz. The solid lines represent fits to the dispersive Hamiltonian model of equation (1) (with noise added; Supplementary Section D), from which we extract an interaction strength $2J/2\pi$ of 11.6 ± 0.2 MHz. **c**, Pulse sequence similar to that in **a**, but starting from |01⟩. **d**, Similar data and fit as in **b**, but starting from |01⟩. Here we extract $2J/2\pi = 11.8 \pm 0.2$ MHz.

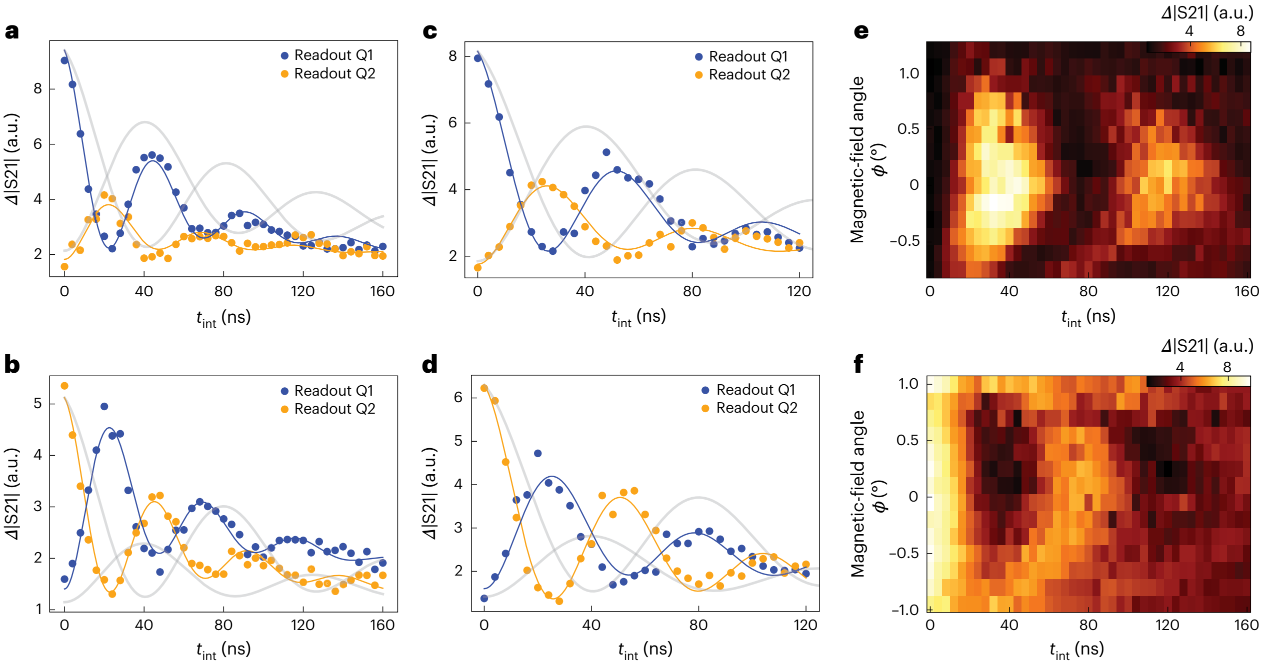

Fig. 4 | Control of iSWAP oscillations. a,**b**, iSWAP oscillations similar to that shown in Fig. 3b,d, with $g_{\mathrm{s},1(2)}/2\pi$ increased to ~31.9 MHz. The fitted oscillation frequencies are now 21.4 ± 0.3 MHz (**a**) and 21.3 ± 0.3 MHz (**b**). **c**,**d**, iSWAP oscillations similar to that shown in Fig. 3b,d, with $g_{\mathrm{s},1(2)}/2\pi$ increased to ~31.9 MHz and $\Delta_{2\mathrm{s},1(2)}/2\pi$ increased to ~89 MHz. Here the fitted frequencies are 18.2 ± 0.4 MHz (**c**) and 18.7 ± 0.3 MHz (**d**). In **a**–**d**, the data points and solid lines represent the measurements and the fit, as shown in Fig. 3. The faint solid lines reproduce the (rescaled) solid lines from Fig. 3, for comparison. The data points in **a**–**d** are averaged for 10^6 times. **e**, iSWAP oscillations as a function of the magnetic-field angle ϕ with $B_{\mathrm{r}} = 52.3$ mT, starting from |01⟩ and reading out qubit 1. A chevron pattern is visible, as discussed in the main text. **f**, iSWAP oscillations as a function of the magnetic-field angle similar to that in **e** but reading out qubit 2. The ϕ axes for **e** and **f** are set to $\phi = 0$ at which the oscillation is the slowest. The actual $\phi = 0$ points do not match, possibly due to a slight difference in the micromagnet magnetization between the measurements for **e** and **f**. The data points in **e** and **f** are averaged for 4.5×10^5 times.

Also, because T_1 is only a factor of 2 to 3 longer than T_2, the oscillations are damped asymmetrically towards the ground state. The unequal visibilities of the readout for the two qubits can be attributed to two causes. First, the dominating reason is that the qubit relaxation times differ, which impacts the signal accumulated during the 400 ns probe interval. Second, the dispersive shift in the resonator frequency has a different magnitude ($\Delta|S21|$) for the two qubits.

Next, we test whether the measured oscillation frequency varies with the control parameters according to equation (2). First, we increase the spin–photon coupling strength $g_{s,1(2)}/2\pi$ from ~21.5 MHz to ~31.9 MHz by reducing the tunnel couplings to ~4.35 GHz, keeping B_{ext} fixed to maintain approximately the same spin–cavity detuning as that shown in Fig. 3. The smaller tunnel coupling decreases the charge–photon detuning, thereby increasing the charge-induced dispersive shift and lowering the resonator frequency. Simultaneously, it reduces the spin frequency, due to increased spin–charge admixing. Therefore, the spin–cavity detuning stays almost the same as before, namely, $\Delta_{2s,1(2)}/2\pi \approx 63$ MHz. As expected, we find an increased oscillation frequency of ~21.4 MHz (Fig. 4a,b). Next, we increase the spin–cavity detuning to $\Delta_{2s,1(2)}/2\pi \approx 89$ MHz by reducing the external magnetic field B_{ext} from 50 mT to 49 mT, and keeping the spin–photon coupling strength the same as that shown in Fig. 4a,b. The angle of the field is re-calibrated to 11.5° to ensure that the two qubits are still on resonance with each other. In this setting, we find that the oscillation frequency is reduced from ~21.4 MHz to ~18.5 MHz (Fig. 4c,d). These fitted oscillation frequencies are slightly different than those predicted using equation (2). We expect that the discrepancy will decrease for a larger Δ_{2s}/g_s ratio, that is, deeply in the dispersive regime (Extended Data Fig. 4 shows the data for $\Delta_{2s}/g_s \approx 5$, 7 and 10). Consistent with this interpretation, the fitted frequencies are in excellent agreement with the values predicted by a more complete simulation, which takes into account the non-zero photon population in the resonator (Extended Data Fig. 3 and Supplementary Section D).

One further control knob is given by the frequency detuning between the two qubits, which can be adjusted via the external-magnetic-field angle B_ϕ. The oscillation frequency is expected to vary according to $\frac{1}{2\pi}\sqrt{(2J)^2 + (\omega_{Q1} - \omega_{Q2})^2}$, where ω_{Qi} are the angular frequencies of the qubits (the spectroscopy data are given elsewhere[26]). As shown in Fig. 4e,f, the measurement results display chevron patterns as a function of the magnetic-field angle and the duration of the two-qubit interaction. For $\omega_{Q1} = \omega_{Q2}$, the oscillation is the slowest and the $|01\rangle$ and $|10\rangle$ populations are maximally interchanged (maximum contrast). When the magnetic-field angle is changed such that ω_{Q1} differs from ω_{Q2}, the rotation axis is tilted in the $|01\rangle/|10\rangle$ subspace and we observe accelerated oscillations but with lower contrast, as expected.

Finally, we apply a calibrated iSWAP oscillation in a practical scenario in which the coherent time evolution of one qubit is transferred to the state of the other qubit. First, a reference experiment is executed (Fig. 5a), where we apply a resonant microwave burst of variable duration to qubit 2 in the flopping-mode regime and read out this qubit (orange data points), similar to that in Fig. 2b. Then, we repeat the same measurement but instead read out qubit 1 (Fig. 5a, blue data points). As shown in Fig. 5, qubit 2 completes a Rabi cycle and qubit 1 remains in the ground state. Next, we perform a similar experiment with a calibrated iSWAP evolution inserted after the microwave burst, which is expected to map the Rabi oscillation of qubit 2 onto qubit 1 by swapping their populations. As shown in Fig. 5b, the coherence expressed by the Rabi oscillation of qubit 2 is now indeed visible in the final state of qubit 1 (blue data points); meanwhile, qubit 2 arrives in the ground state, which is the initial state of qubit 1 (orange data points).

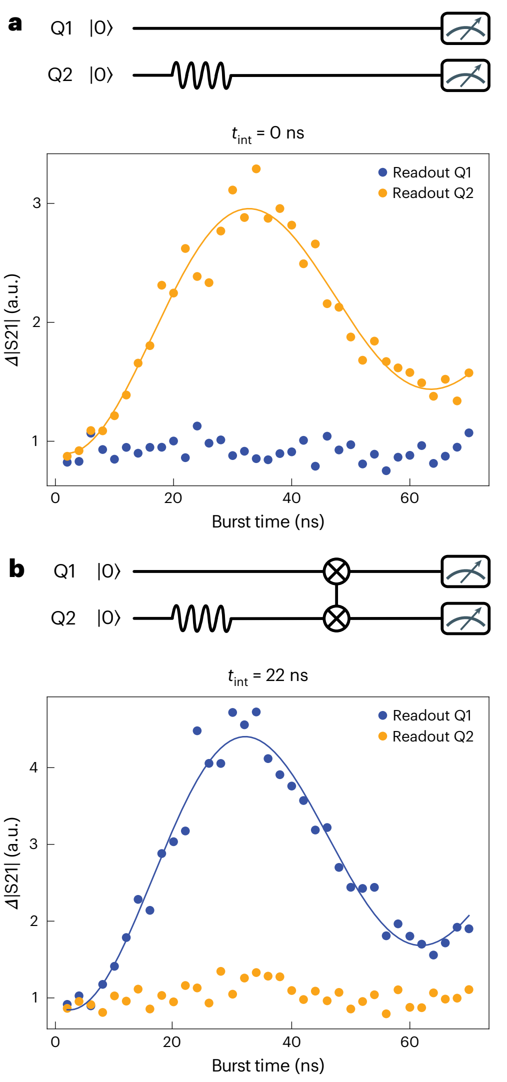

Fig. 5 | Swapped Rabi-cycle experiment. a, Rabi oscillation of qubit 2 serving as a reference experiment. Starting with both spins in the ground state, a microwave burst of variable duration is applied to qubit 2 followed by the read out of this qubit (next, the experiment is repeated and qubit 1 is read). The data points and solid lines represent the measurement and a fit to a sinusoid, as shown in Fig. 2. Each data point is averaged for 5×10^5 times. **b**, Rabi oscillation of qubit 2 detected through qubit 1. After the microwave burst is applied to qubit 2, a calibrated iSWAP evolution is executed before read out (performed as that in **a**).

Conclusion

Looking ahead, we aim to increase the quality factor of the oscillations in several ways. First, the charge qubit linewidth of ~60 MHz is much larger than that in state-of-the-art devices, where linewidths down to 2.6 MHz have been reported[44]. Given the admixing of the charge and spin degrees of freedom needed for spin–photon coupling, a narrower charge qubit linewidth immediately translates to a narrower spin qubit linewidth. Furthermore, the ~30 MHz spin–photon coupling strength can be enhanced to at least ~300 MHz via both stronger lever arms, higher resonator impedance and stronger intrinsic or engineered spin–orbit coupling[45]. Combining these will allow application in the deep dispersive regime without compromising on the gate speed. With this and a modest improvement in the resonator linewidth of 0.3 MHz, a >99% two-qubit gate fidelity should be within reach[22].

Furthermore, high-fidelity single-qubit operation can be achieved by conventional electric-dipole spin resonance with the electron in a single dot[46]. Spin readout can be improved by including a third (auxiliary) dot for spin-to-charge conversion based on Pauli-spin blockade, enabling rapid and high-fidelity single-shot readout through the resonator[47]. With a dedicated readout resonator or a sensing dot, readout and two-qubit gates can be individually optimized. Scaling up the present two-qubit interaction requires local spin-frequency control and tunability, allowing the qubit frequencies to be individually tuned. Alternatively, the present architecture also allows for exploring two-qubit gates based on cross-resonance coupling or in the longitudinal-coupling regime.[48–51]

These results mark an important milestone in the effort towards the creation of on-chip networks of spin qubit registers. The increased interaction distance between qubits allows for the co-integration of classical electronics and for overcoming the wiring bottleneck. The networked qubit connectivity calls for the design of optimized quantum error correction codes. Moreover, this platform opens up new possibilities in quantum simulation involving both fermionic and bosonic degrees of freedom.

Online content

Any methods, additional references, Nature Portfolio reporting summaries, source data, extended data, supplementary information, acknowledgements, peer review information; details of author contributions and competing interests; and statements of data and code availability are available at https://doi.org/10.1038/s41567-024-02694-8.

References

1. Meter, R. V. & Horsman, C. A blueprint for building a quantum computer. *Commun. ACM* **56**, 84 (2013).
2. Monroe, C. R., Schoelkopf, R. J. & Lukin, M. D. Quantum connections. *Sci. Am.* **314**, 50 (2016).
3. Loss, D. & DiVincenzo, D. P. Quantum computation with quantum dots. *Phys. Rev. A* **57**, 120 (1998).
4. Burkard, G., Ladd, T. D., Pan, A., Nichol, J. M. & Petta, J. R. Semiconductor spin qubits. *Rev. Mod. Phys.* **95**, 025003 (2023).
5. Maurand, R. et al. A CMOS silicon spin qubit. *Nat. Commun.* **7**, 13575 (2016).
6. Zwerver, A. M. et al. Qubits made by advanced semiconductor manufacturing. *Nat. Electron.* **5**, 184 (2022).
7. Vandersypen, L. M. K. et al. Interfacing spin qubits in quantum dots and donors—hot, dense, and coherent. *npj Quantum Inf.* **3**, 1 (2017).
8. Petta, J. R. et al. Coherent manipulation of coupled electron spins in semiconductor quantum dots. *Science* **309**, 2180 (2005).
9. Taylor, J. M. et al. Fault-tolerant architecture for quantum computation using electrically controlled semiconductor spins. *Nat. Phys.* **1**, 177 (2005).
10. Baart, T. A., Fujita, T., Reichl, C., Wegscheider, W. & Vandersypen, L. M. K. Coherent spin-exchange via a quantum mediator. *Nat. Nanotechnol.* **12**, 26 (2016).
11. Fedele, F. et al. Simultaneous operations in a two-dimensional array of singlet-triplet qubits. *PRX Quantum* **2**, 040306 (2021).
12. Shulman, M. D. et al. Demonstration of entanglement of electrostatically coupled singlet-triplet qubits. *Science* **336**, 202 (2012).
13. Fujita, T., Baart, T. A., Reichl, C., Wegscheider, W. & Vandersypen, L. M. K. Coherent shuttle of electron-spin states. *npj Quantum Inf.* **3**, 1 (2017).
14. Flentje, H. et al. Coherent long-distance displacement of individual electron spins. *Nat. Commun.* **8**, 501 (2017).
15. Jadot, B. et al. Distant spin entanglement via fast and coherent electron shuttling. *Nat. Nanotechnol.* **16**, 570 (2021).
16. Blais, A., Grimsmo, A. L., Girvin, S. M. & Wallraff, A. Circuit quantum electrodynamics. *Rev. Mod. Phys.* **93**, 025005 (2021).
17. Burkard, G., Gullans, M. J., Mi, X. & Petta, J. R. Superconductor-semiconductor hybrid-circuit quantum electrodynamics. *Nat. Rev. Phys.* **2**, 129 (2020).
18. Mi, X. et al. A coherent spin-photon interface in silicon. *Nature* **555**, 599 (2018).
19. Samkharadze, N. et al. Strong spin-photon coupling in silicon. *Science* **359**, 1123 (2018).
20. Landig, A. J. et al. Coherent spin-photon coupling using a resonant exchange qubit. *Nature* **560**, 179 (2018).
21. Borjans, F., Croot, X. G., Mi, X., Gullans, M. J. & Petta, J. R. Resonant microwave-mediated interactions between distant electron spins. *Nature* **577**, 195 (2019).
22. Benito, M., Petta, J. R. & Burkard, G. Optimized cavity-mediated dispersive two-qubit gates between spin qubits. *Phys. Rev. B* **100**, 81412 (2019).
23. Warren, A., Güngördü, U., Kestner, J. P., Barnes, E. & Economou, S. E. Robust photon-mediated entangling gates between quantum dot spin qubits. *Phys. Rev. B* **104**, 115308 (2021).
24. Majer, J. et al. Coupling superconducting qubits via a cavity bus. *Nature* **449**, 443 (2007).
25. Sillanpää, M. A., Park, J. I. & Simmonds, R. W. Coherent quantum state storage and transfer between two phase qubits via a resonant cavity. *Nature* **449**, 438 (2007).
26. Harvey-Collard, P. et al. Coherent spin-spin coupling mediated by virtual microwave photons. *Phys. Rev. X* **12**, 021026 (2022).
27. Orphal-Kobin, L., Torun, C. G., Bopp, J. M., Pieplow, G., and Schröder, T. Coherent microwave, optical, and mechanical quantum control of spin qubits in diamond. *Adv. Quantum Technol.* 2300432 (2024).
28. Heindel, T., Kim, J.-H., Gregersen, N., Rastelli, A. & Reitzenstein, S. Quantum dots for photonic quantum information technology. *Adv. Opt. Photon.* **15**, 613 (2023).
29. Viennot, J. J., Dartiailh, M. C., Cottet, A. & Kontos, T. Coherent coupling of a single spin to microwave cavity photons. *Science* **349**, 408 (2015).
30. Benito, M. et al. Electric-field control and noise protection of the flopping-mode spin qubit. *Phys. Rev. B* **100**, 125430 (2019).
31. Croot, X. et al. Flopping-mode electric dipole spin resonance. *Phys. Rev. Res.* **2**, 012006 (2020).
32. Samkharadze, N. et al. High-kinetic-inductance superconducting nanowire resonators for circuit QED in a magnetic field. *Phys. Rev. Appl.* **5**, 044004 (2016).
33. Harvey-Collard, P. et al. On-chip microwave filters for high-impedance resonators with gate-defined quantum dots. *Phys. Rev. Appl.* **14**, 034025 (2020).
34. van Woerkom, D. J. et al. Microwave photon-mediated interactions between semiconductor qubits. *Phys. Rev. X* **8**, 041018 (2018).
35. Benito, M., Mi, X., Taylor, J. M., Petta, J. R. & Burkard, G. Input-output theory for spin-photon coupling in Si double quantum dots. *Phys. Rev. B* **96**, 235434 (2017).
36. Hu, X., Liu, Y. X. & Nori, F. Strong coupling of a spin qubit to a superconducting stripline cavity. *Phys. Rev. B* **86**, 035314 (2012).
37. Pioro-Ladrière, M. et al. Electrically driven single-electron spin resonance in a slanting Zeeman field. *Nat. Phys.* **4**, 776 (2008).
38. Macklin, C. et al. A near-quantum-limited Josephson traveling-wave parametric amplifier. *Science* **350**, 307 (2015).
39. Stano, P. & Loss, D. Review of performance metrics of spin qubits in gated semiconducting nanostructures. *Nat. Rev. Phys.* **4**, 672 (2022).
40. Bienfait, A. et al. Controlling spin relaxation with a cavity. *Nature* **531**, 74 (2016).
41. Yan, F. et al. Distinguishing coherent and thermal photon noise in a circuit quantum electrodynamical system. *Phys. Rev. Lett.* **120**, 260504 (2018).
42. Tavis, M. & Cummings, F. W. Exact solution for an *n*-molecule-radiation-field Hamiltonian. *Phys. Rev.* **170**, 379 (1968).
43. Burkard, G. & Imamoglu, A. Ultra-long-distance interaction between spin qubits. *Phys. Rev. B* **74**, 41307 (2006).

44. Mi, X., Cady, J. V., Zajac, D. M., Deelman, P. W. & Petta, J. R. Strong coupling of a single electron in silicon to a microwave photon. *Science* **355**, 156 (2017).
45. Yu, C. X. et al. Strong coupling between a photon and a hole spin in silicon. *Nat. Nanotechnol.* **18**, 741 (2023).
46. Yoneda, J. et al. A quantum-dot spin qubit with coherence limited by charge noise and fidelity higher than 99.9%. *Nat. Nanotechnol.* **13**, 102 (2017).
47. Zheng, G. et al. Rapid gate-based spin read-out in silicon using an on-chip resonator. *Nat. Nanotechnol.* **14**, 742 (2019).
48. Beaudoin, F., Lachance-Quirion, D., Coish, W. A. & Pioro-Ladrière, M. Coupling a single electron spin to a microwave resonator: controlling transverse and longitudinal couplings. *Nanotechnology* **27**, 464003 (2016).
49. Corrigan, J. et al. Longitudinal coupling between a Si/Si1−*x*Ge*x* double quantum dot and an off-chip TiN resonator. *Phys. Rev. Appl.* **20**, 064005 (2023).
50. Bøttcher, C. G. et al. Parametric longitudinal coupling between a high-impedance superconducting resonator and a semiconductor quantum dot singlet-triplet spin qubit. *Nat. Commun.* **13**, 4773 (2022).
51. Rigetti, C. & Devoret, M. Fully microwave-tunable universal gates in superconducting qubits with linear couplings and fixed transition frequencies. *Phys. Rev. B* **81**, 134507 (2010).
52. Dijkema, J. et al. Source data of the publication: Cavity-mediated iSWAP oscillations between distant spins. Version 3. *4TU. ResearchData* https://doi.org/10.4121/6c34cc01-bbab-4f7c-b2e8-6fab5f07020d.v3 (2024).

Data availability

Data supporting this work are available via 4TU.ResearchData at https://doi.org/10.4121/6c34cc01-bbab-4f7c-b2e8-6fab5f07020d.v3 (ref. [52]). Source data are provided with this paper.

Code availability

Codes used for data processing and numerical simulations are available via 4TU.ResearchData at https://doi.org/10.4121/6c34cc01-bbab-4f7c-b2e8-6fab5f07020d.v3 (ref. [52]).

Acknowledgements

We thank W. Oliver for providing the travelling-wave parametric amplifier; T. Bonsen for helpful insights involving input–output simulations; L. P. Kouwenhoven and his team for access to the NbTiN film deposition; F. A. Carrasco for assistance with the sample fabrication; L. DiCarlo and his team for access to the ^{3}He cryogenic system; O. Benningshof, R. Schouten and R. Vermeulen for technical assistance; and other members of the spin qubit team at QuTech for useful discussions. This research was supported by the European Union's Horizon 2020 research and innovation programme under grant agreement no. 951852 (QLSI project), the European Research Council (ERC Synergy Quantum Computer Lab), the Dutch Ministry for Economic Affairs through the allowance for Topconsortia for Knowledge and Innovation (TKI) and the Netherlands Organization for Scientific Research (NWO/OCW) as part of the Frontiers of Nanoscience (NanoFront) program. X.X. acknowledges support from the Dutch Research Council (NWO) via the National Growth Fund program Quantum Delta NL (grant no. NGF.1623.23.024).

Author contributions

J.D. and X.X. performed the experiment and analysed the data with help from M.R.-R. M.R.-R. developed the theory model. P.H.-C. fabricated the device. S.L.d.S. and G.Z. contributed to the preparation of the experiment. G.S. supervised the development of the Si/SiGe heterostructure, grown by A.S. and designed by A.S and G.S. J.D., X.X. and L.M.K.V. conceived the project. L.M.K.V. supervised the project. J.D., X.X., M.R.-R. and L.M.K.V. wrote the manuscript with input from all authors.

Competing interests

The authors declare no competing interests.

Additional information

Extended data is available for this paper at https://doi.org/10.1038/s41567-024-02694-8.

Supplementary information The online version contains supplementary material available at https://doi.org/10.1038/s41567-024-02694-8.

Correspondence and requests for materials should be addressed to Lieven M. K. Vandersypen.

Peer review information *Nature Physics* thanks the anonymous reviewers for their contribution to the peer review of this work.

Reprints and permissions information is available at www.nature.com/reprints.

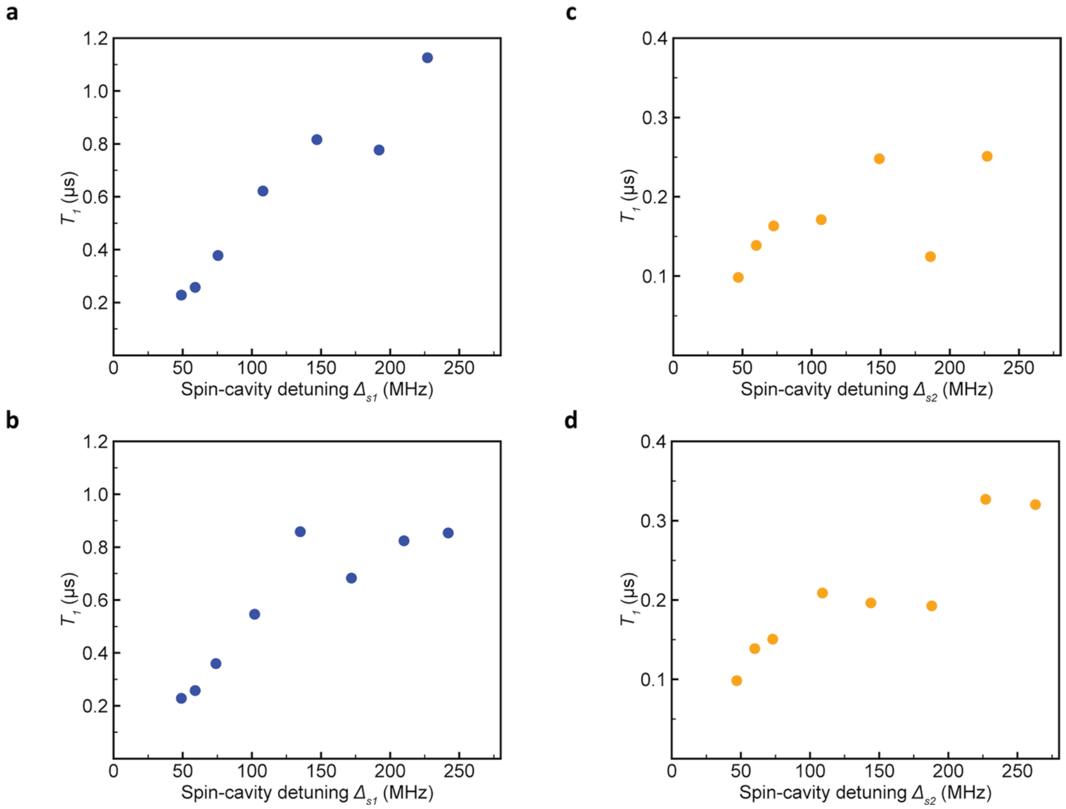

Extended Data Fig. 1 | Relaxation time T_1 as a function of spin-cavity detuning Δ_s with the cavity loaded with one charge only. a,c. Measured T_1 of qubit 1(**a**) and 2(**c**) as function of Δ_s while recalibrating the magnetic field angle β_ϕ for every Δ_s value in order to maintain the two spin frequencies approximately equal for all T_1 measurements. **b,d**. Measured T_1 of qubit 1(**b**) and 2(**d**) as function of Δ_s with the calibrated angle of $\beta_\phi = 10^\circ$ to equalize the spin frequencies at a $\Delta_{s,1(2)}$ of 50 MHz and leaving it unchanged for all other T_1 measurements. Since the Purcell decay rate is proportional to $g_{s,1(2)}^2/\Delta_{s,1(2)}^2$, its effect should be similar for both qubits since we have $g_{s,1} \approx g_{s,2}$ and $\Delta_{s,1} \approx \Delta_{s,2}$. We observe that the measured T_1 time indeed degrades for smaller spin-cavity detuning, which is a sign of Purcell-decay. However, even though the qubits share the same spin-cavity detuning and spin-photon coupling, the measured T_1 times of the two qubits differ by up to a factor of 4. Therefore, we suspect Purcell decay to have an influence on the relaxation time but do not expect it to be the only source of T_1 decay. Note that these data are collected in a separate cool-down from the numbers measured in Table S1, which explains the difference between them.

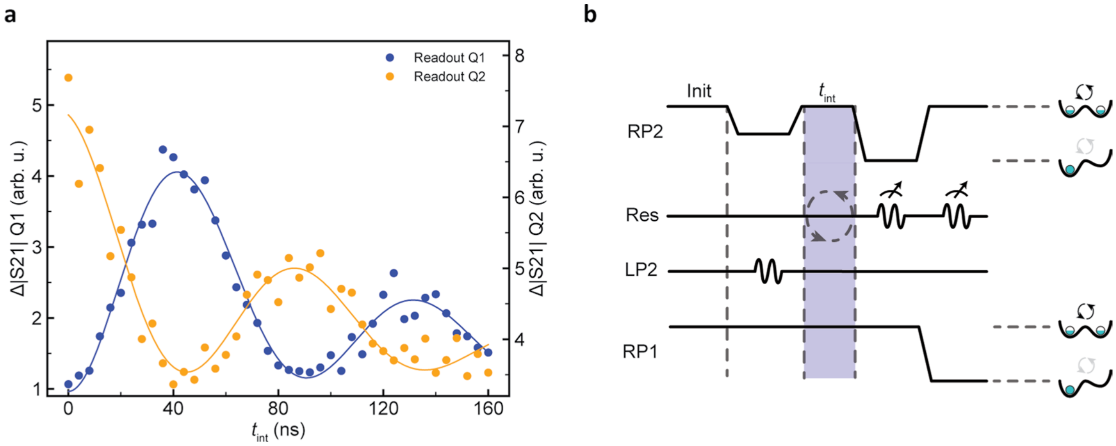

Extended Data Fig. 2 | SWAP oscillations between the two distant spins, using single-dot EDSR instead of the flopping-mode regime to excite qubit 2. a. The operation regime is similar as in Fig. 3b,d, with $g_{s,1(2)}/2\pi \approx 21.5$ MHz and $\Delta_{2s,1(2)}/2\pi \approx 65.5$ MHz. The solid lines represent fits to the dispersive Hamiltonian model of Eq. (1), from which we extract an interaction strength $2J/2\pi$ of 11.1 MHz. Note the visibility of qubit 2 is off-set compared to all other measurements (both traces being plotted on different scales). The exact mechanism is unknown, but we have verified that it is caused by the increased power of the microwave burst necessary to drive the qubit in a single dot. Each data point is averaged for 10^6 times. **b**. Pulse sequence similar to Fig. 3a, with the difference being that the MW drive is now resonant with qubit 2 when pulsed to a single dot, to prepare $|01\rangle$. The data points in **a** are averaged for 10^6 times.

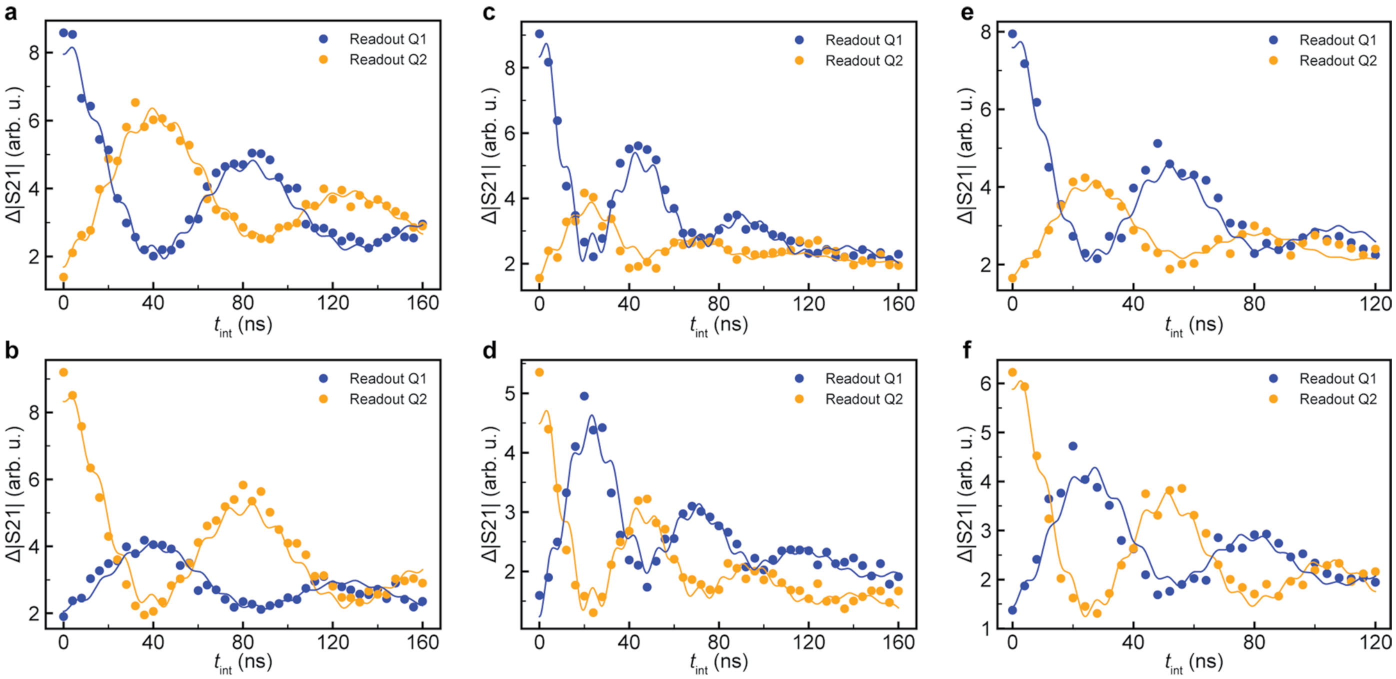

Extended Data Fig. 3 | Two-qubit interaction data fitted with the full model. The rapid oscillations arising from the fits are due to coherent energy exchange with the resonator via residual vacuum Rabi oscillations. The fitted spin-photon coupling strength $g_s/2\pi$, the spin-spin interaction strength $2J/2\pi$ and the estimated fidelities for the $\sqrt{\text{iSWAP}}$ gate $F_{\sqrt{\text{iSWAP}}}$ and the iSWAP gate FiSWAP are given hereby.
a. $g_s/2\pi = 20.9$ MHz, $2J/2\pi = 11.5$ MHz, $F_{\sqrt{\text{iSWAP}}} = 82.2\%$, $F_{\text{iSWAP}} = 67.4\%$.
b. $g_s/2\pi = 21.0$ MHz, $2J/2\pi = 11.6$ MHz, $F_{\sqrt{\text{iSWAP}}} = 84.0\%$, $F_{\text{iSWAP}} = 72.2\%$.
c. $g_s/2\pi = 29.7$ MHz, $2J/2\pi = 21.2$ MHz, $F_{\sqrt{\text{iSWAP}}} = 76.5\%$, $F_{\text{iSWAP}} = 62.0\%$.
d. $g_s/2\pi = 29.4$ MHz, $2J/2\pi = 20.9$ MHz, $F_{\sqrt{\text{iSWAP}}} = 77.5\%$, $F_{\text{iSWAP}} = 63.2\%$
e. $g_s/2\pi = 31.0$ MHz, $2J/2\pi = 18.0$ MHz, $F_{\sqrt{\text{iSWAP}}} = 80.6\%$, $F_{\text{iSWAP}} = 66.2\%$
f. $g_s/2\pi = 31.6$ MHz, $2J/2\pi = 18.7$ MHz, $F_{\sqrt{\text{iSWAP}}} = 82.5\%$, $F_{\text{iSWAP}} = 70.3\%$.
The estimated $\sqrt{\text{iSWAP}}$ gate fidelity reported in the main text is an average over the the numbers from **a** and **b**.

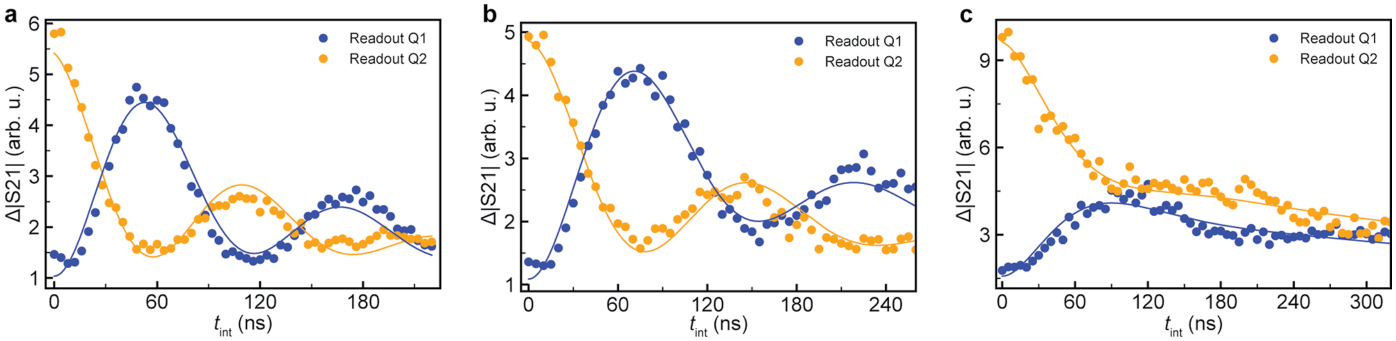

Extended Data Fig. 4 | iSWAP oscillations between the two distant spins for increasing $\boldsymbol{\beta = \Delta_{2s}/g_d}$. a–c. The spin-photon coupling $g_{s,1(2)}/2\pi$ is similar as in Fig. 3 for all panels (~ 21.5 MHz), but $\Delta_{s,1(2)}/2\pi$ is changed to 110 MHz (β ~ 5), 150 MHz (β ~ 7) and 220 MHz (β ~ 10) for **a**–**c**, respectively. The solid lines represent fits to the dispersive Hamiltonian model of Eq. (1), from which we extract the respective interaction strengths $2J/2\pi$ of 8.7 MHz, 6.7 MHz and 5.6 MHz. For $\beta = 10$, not only the oscillation is slower compared the case of $\beta = 3$, but the spin dephasing time was reduced to 20–25 ns in this case, for reasons that are unclear (perhaps a charge fluctuator was activated here). This results in a significantly damped oscillation which makes it difficult to perform a proper fit as one can observe in panel **c**. The data points in **a,c** are averaged for $3 \cdot 10^6$ times and in **b** for $2 \cdot 10^6$ times.